








Thermoelectric properties and electronic structure of Cr(Mo, V)N_x thin films studied by synchrotron and lab-based x-ray spectroscopy

Susmita Chowdhury ^{*}, Victor Hjort , Rui Shu , Grzegorz Greczynski , Arnaud le Febvrier ,
Per Eklund , and Martin Magnuson 

*Thin Film Physics Division, Department of Physics, Chemistry and Biology (IFM),
Linköping University, Linköping SE-581 83, Sweden*



(Received 25 August 2023; revised 28 September 2023; accepted 18 October 2023; published 15 November 2023)

Chromium-based nitrides are used in hard, resilient coatings and show promise for thermoelectric applications due to their combination of structural, thermal, and electronic properties. Here, we investigate the electronic structures and chemical bonding correlated to the thermoelectric properties of epitaxially grown chromium-based multicomponent nitride Cr(Mo, V)N_x thin films. The small amount of N vacancies causes Cr 3*d* and N 2*p* states to appear at the Fermi level and reduces the band gap in Cr_{0.51}N_{0.49}. Incorporating holes by alloying of V in N-deficient CrN results in an enhanced thermoelectric power factor with marginal change in the charge transfer of Cr to N compared with Cr_{0.51}N_{0.49}. Further alloying of Mo, isoelectronic to Cr, increases the density of states at the Fermi level due to hybridization of the (Cr, V) 3*d* and Mo 4*d*-N 2*p* states in Cr(Mo, V)N_x. This hybridization and N off-stoichiometry result in more metal-like electrical resistivity and reduction in Seebeck coefficient. The N deficiency in Cr(Mo, V)N_x also depicts a critical role in reduction of the charge transfer from metal to N site compared with Cr_{0.51}N_{0.49} and Cr_{0.50}V_{0.03}N_{0.47}. In this paper, we envisage ways for enhancing thermoelectric properties through electronic band engineering by alloying and competing effects of N vacancies.

DOI: [10.1103/PhysRevB.108.205134](https://doi.org/10.1103/PhysRevB.108.205134)

I. INTRODUCTION

Chromium nitride (CrN) is important in a range of existing and prospective applications due to its combination of structural, mechanical, magnetic, and electronic properties [1]. CrN undergoes a magnetostructural transition from a paramagnetic B1 NaCl (rocksalt) type of structure (*Fm* $\bar{3}$ *m*) at room temperature to an antiferromagnetic orthorhombic structure (*Pnma*) at ~ 260 – 285 K temperature regime [2–4] accompanied by a debatable semiconducting/insulating-to-metallic transition [4–6]. Given that CrN is based on abundant and relatively cheap raw materials, it is promising for large-scale production, and CrN-based thin films have long been in use in hard-coating applications [7–9].

Conventional thermoelectric materials such as tellurides and antimonides are used to harvest thermoelectric power from waste energy [10–12] but are limited because of scarcity and toxicity of the constituent elements [13,14]. An emerging class of alternative materials are transition metal nitrides, particularly those based on ScN and CrN [15,16]. With a thermoelectric power factor of 1.5 – 5 mW m⁻¹ K⁻² and relatively low thermal conductivity of 2 – 4 W m⁻¹ K⁻¹ due to strong

spin-lattice coupling [17,18], CrN is comparable with conventional Bi₂Te₃ and PbTe [1,19]. Thermoelectric properties, i.e., the Seebeck coefficient (*S*), electrical conductivity (σ), and thermal conductivity (κ) are strongly coupled and hence hard to optimize. Generally, reducing dimensionality of materials, inducing defects (hole/electron doping or grain boundaries) by alloying, or tuning the atomic masses of alloying elements are alternatives to improve the thermoelectric properties of the parent compound [20–23]. Moreover, inducing point defects (vacancy, impurity, or interstitial) could further reduce the thermal conductivity by increasing the phonon scattering as has been observed for other traditional thermoelectric materials [24–26]. The generalized findings are valid for chromium-based multicomponent nitrides compared with binary CrN, manifesting higher hardness [27], thermal stability [28], and enhanced thermoelectric performances [29].

However, the thermoelectric performances are strongly correlated to the electronic structure of the final compound. Theoretical band structure calculations reveal a local and sharp increase of the density of states (DOS) near the Fermi level (E_F) for any thermoelectric materials [30]. Hence, to gain improved power factor ($S^2\sigma$), the DOS should be as large as possible around E_F for increased σ and as asymmetric as possible to achieve the best *S* [31]. It occurs due to the resonance of either the valence or conduction band of the host semiconductor with an energy level of the localized atom in the compound and can be explained to a first approximation by the Mott equation [21,30]:

$$S = \frac{\pi^2 k_B^2 T}{3q} \left[\frac{d\{\ln \sigma(E)\}}{dE} \right]_{E=E_F}, \quad (1)$$

*susmita.chowdhury@liu.se

Published by the American Physical Society under the terms of the [Creative Commons Attribution 4.0 International license](https://creativecommons.org/licenses/by/4.0/). Further distribution of this work must maintain attribution to the author(s) and the published article's title, journal citation, and DOI. Funded by *Bibsam*.

where k_B = Boltzmann constant, q = charge, and T = absolute temperature. The expression for $\sigma(E)$ is given by [21]

$$\sigma(E) = n(E)q\mu(E). \quad (2)$$

Here, $n(E)$ = charge carrier density, and $\mu(E)$ = mobility of the charge carrier. The charge carrier density is related to the DOS $g(E)$ and Fermi function $f(E)$ as [21]

$$n(E) = g(E)f(E). \quad (3)$$

Furthermore, theoretical approaches for strongly correlated electron systems like CrN indicate that induced defects (metal/N vacancies) lead to an increase in the DOS along with a shift in E_F affecting the band opening [32]. This in turn affects the thermoelectric power factor $S^2\sigma$ [32,33]. Among different alloying elements (e.g., Sc, V, Al, Mo, and W) in CrN, V alloying resulted in enhanced thermoelectric properties of $\text{Cr}_{1-x}\text{V}_x\text{N}$ in both bulk and thin films due to increased hole concentration [34,35]. While alloying heavier Mo atoms, isoelectronic to Cr, would not alter the electronic properties substantially, it would rather affect thermal transport properties by increased phonon scattering [36].

Consequently, in this paper, attempts were made to synthesize epitaxial CrN, $\text{Cr}_{1-x}\text{V}_x\text{N}$ and $\text{Cr}(\text{Mo},\text{V})\text{N}$ thin films. Literature on such a complex chromium-based multicomponent nitride $\text{Cr}(\text{Mo},\text{V})\text{N}_x$ is lacking. Since probing the electronic structure in any thermoelectric material is primordial for further improvement of transport properties, below the E_F , the DOS was probed by synchrotron-based resonant inelastic x-ray scattering [RIXS; partial DOS (p-DOS)] complementary to lab-based valence band spectroscopy (VBS; total DOS). RIXS studies on correlated chromium nitride-based system is lacking, possibly due to poor energy resolution in earlier times [37]. The valence band below E_F was also studied using lab-based x-ray photoelectron spectroscopy (XPS) which is highly surface sensitive with overlapping spectral features. In addition, above E_F , synchrotron-based x-ray absorption (XAS) measurements were performed, probing the unoccupied states in the conduction band. To investigate the thermoelectric properties, electrical resistivity and the Seebeck coefficients of the samples were measured at room temperature. Thus, the structural, electronic, and thermoelectric correlations were systematically and quantitatively studied for CrN and $\text{Cr}_{1-x}\text{V}_x\text{N}$ thin films. Later, we qualitatively delve into the more complex systems of chromium-based multicomponent nitride $\text{Cr}(\text{Mo},\text{V})\text{N}_x$ thin films.

II. EXPERIMENTAL DETAILS

CrN, $\text{Cr}_{1-x}\text{V}_x\text{N}$, and a series of $\text{Cr}(\text{Mo},\text{V})\text{N}_x$ thin film samples were deposited on single-side polished *c*-plane sapphire (0001) substrates using reactive dc magnetron sputtering in an ultrahigh-vacuum deposition system described elsewhere [38]. The substrates were left electrically floating at a deposition temperature of 600°C. Depositions were performed using three magnetrons, each with >99.7% pure metal targets and in an atmosphere of Ar and N₂. The gas composition was fixed at 40% Ar and 60% N₂. The CrN reference was deposited at 0.32 Pa and 22 sccm Ar, while the rest of the samples were deposited at 0.40 Pa and 28 sccm Ar due to

difficulty in sustaining the plasma of all three targets ignited at lower gas flow. More detailed description of depositions and more in-depth characterization can be found elsewhere [39].

Rutherford backscattering (RBS) measurements were performed at Uppsala University using a 2 MeV ⁴He⁺ ion beam [40]. Backscattered ions were detected at a scattering angle of 170°. Channeling effects in the substrates and samples were minimized by adjusting the equilibrium incidence angle to 5° with respect to the surface normal and performing multiple small random angular movements within a range of 2° during data acquisition. Atomic concentrations were extracted from the spectra using the SIMNRA simulation program [41]. The time-of-flight elastic recoil detection analysis measurements were also done and discussed in the Supplemental Material [42].

The x-ray diffraction (XRD) measurements were performed in Bragg-Brentano mode (θ - 2θ) using a PANalytical X'Pert Pro diffractometer system, with a Cu-K α source operated at 45 kV and 40 mA. The incident optics was a Bragg-Brentano module with 0.5° divergence slit and a 0.5° antiscatter slit, while the diffracted optics included a 5.0 mm antiscatter slit, a 0.04 rad Soller slit, a Ni-filter, and an X'Celerator detector. Detailed structural analysis using pole figures and transmission electron microscopy is described elsewhere [39].

The soft x-ray absorption near-edge structure (XANES) at Cr 2*p*, N 1*s*, Mo 3*p*, and V 2*p* was measured at the SPECIES beamline equipped with an elliptically polarizing undulator (EPU61) and a plane grating monochromator, at the MAX IV Laboratory, Lund, Sweden. The XANES spectra were measured at 20° grazing incidence with 0.1 eV resolution using total electron yield and total fluorescence yield, simultaneously. The combination of drain current and near edge x-ray absorption fine structure (NEXAFS) detector enabled us to acquire both surface and bulk sensitive information simultaneously. For normalization of the data, a 4- μm -thick Au reference foil was scanned in the same energy range as the samples over each absorption edge.

The RIXS spectra were also measured at the SPECIES beamline with a high-resolution Rowland-mount grazing-incidence grating spectrometer [43,44] with a two-dimensional multichannel detector with a resistive anode readout. The energy resolutions of the monochromator at Cr 2*p* and N 1*s* were 0.45 and 0.2 eV, respectively. The spectrometer resolutions were 0.4 eV for Cr 2*p* and 0.3 eV for N 1*s* spectra. All measurements were performed with a base pressure $<6.7 \times 10^{-7}$ Pa. To minimize self-absorption effects [45], the angle of incidence was 20° from the surface plane during the emission measurements. The x-ray photons were detected parallel to the polarization vector of the incoming beam to minimize elastic scattering.

The hard XANES and extended x-ray absorption fine structure (EXAFS) measurements were performed at the Cr *K* edge in fluorescence mode at the BALDER beamline [46] at MAX IV. For reference and energy calibration, both XANES and EXAFS were performed on a 5- μm -thick Cr foil (*K* edge at 5989 eV) in transmission mode. The energy scans were done using a Si (111) double crystal monochromator, and either a 7-element silicon drift detector (for fluorescence signal) or ionization gas detector filled with Ar, N₂, and He gases

TABLE I. Details of metal film composition obtained from RBS. The lattice parameters were calculated from the 111 peaks of each sample. The absorption edges around the Cr *K*-edge spectra are also listed.

Samples	Film composition RBS (% of Me) ($\pm 1\%$)					Lattice Parameter (± 0.004) (\AA)	Absorption Edge (eV)
	Cr	Mo	V	N	N/Me ratio		
$\text{Cr}_{0.51}\text{N}_{0.49}$	51	–	–	49	0.96	4.159	5997.9
$\text{Cr}_{0.50}\text{V}_{0.03}\text{N}_{0.47}$	50	–	3	47	0.89	4.148	5997.7
$\text{Cr}_{0.44}\text{Mo}_{0.08}\text{V}_{0.06}\text{N}_{0.42}$	44	8	6	42	0.72	4.072	5997
$\text{Cr}_{0.45}\text{Mo}_{0.09}\text{V}_{0.07}\text{N}_{0.40}$	44.5	8.5	7	40	0.67	4.061	5997
$\text{Cr}_{0.44}\text{Mo}_{0.09}\text{V}_{0.08}\text{N}_{0.39}$	44	9	8	39	0.64	4.030	5996.3

(for transmission signal) was used to measure the signals. In fluorescence mode, the samples were placed at an incidence and exit angle of 45° from the source and detector. However, in the transmission mode, the Cr foil was fixed at 90° incidence angle. For both XANES and EXAFS, the energy scans were repeated three times for each sample, at an energy interval of 0.25 and 0.5 eV with an integration time of 0.02 s. For fitting the EXAFS spectra, scattering lengths of the photoelectron and the phase shift were calculated using the FEFF9 code [47,48] considering the body-centered cubic (bcc) and NaCl rock-salt-type B1 structure of Cr (COD-ID 5000220) and CrN (COD-ID 1010974), respectively. The data processing was done using the VIPER software [49], and three scans for each spectrum from the seven channels of the detector were analyzed and summed in the software to generate the final spectrum for each sample. A modified Victoreen polynomial function was used for the pre-edge normalization, and a smoothing spline function was used for the postedge background correction of the x-ray absorption fine structure (XAFS) spectra. The k^2 -weighted Back Fourier transform (BFT) spectra were fitted in the range of $0-13.5 \text{ \AA}^{-1}$ after extracting from the forward FT spectra within $R - \varphi = 1-3 \text{ \AA}$.

Core-level XPS measurements were performed in an Axis Ultra DLD instrument, Kratos Analytical (UK), using monochromatized Al- $K\alpha$ radiation (1486.6 eV). The base pressure during analysis was $\sim 1.3 \times 10^{-7}$ Pa. Prior to measurements, samples were sputter etched for 10 min using 0.5 keV Ar^+ ions at an incident angle of 70° from the surface normal. The area affected by the Ar^+ beam was $3 \times 3 \text{ mm}^2$, while the analysis area was $0.3 \times 0.7 \text{ mm}^2$ (centered in the middle of the etched crater). All spectra are charge referenced by setting the low-energy DOS cutoff at 0 eV. For $\text{Cr}_{0.44}\text{Mo}_{0.08}\text{V}_{0.06}\text{N}_{0.42}$ and $\text{Cr}_{0.45}\text{Mo}_{0.09}\text{V}_{0.07}\text{N}_{0.40}$ samples, an electron flood gun was used to neutralize the charge accumulation on the sample surface due to low electrical conductivity. Complementary to p-DOS, the total DOS was probed using VBS.

The sheet resistances of the samples were measured using a standard four-point probe setup (Jandel Model RM3000) at room temperature (~ 300 K) with equidistant probes with spacing of 1 mm each and a tip radius of 100 μm . The electrical resistivities (ρ_{el}) of the samples were then calculated considering the film thickness [50] as deduced from the x-ray reflectometry measurements (Table S2 in the Supplemental Material [42]). The Seebeck coefficients were also measured at room temperature using a home-built thermoelectric mea-

surement setup [51]. The setup was equipped with two Peltier heat sources for creating a temperature gradient in the sample and two K-type thermocouples for measuring the temperature. The two electrodes were made of Cu and were in contact with the sample in an area of $\sim 9 \times 1 \text{ mm}^2$ in which the K-type thermocouples were present.

III. RESULTS AND DISCUSSION

A. Compositional analysis

Table I shows the compositional analysis of $\text{Cr}_{0.51}\text{N}_{0.49}$, $\text{Cr}_{0.50}\text{V}_{0.03}\text{N}_{0.47}$, and $\text{Cr}(\text{Mo}, \text{V})\text{N}_x$ samples measured by RBS. The composition of the films deduced by fitting revealed substoichiometry in nitrogen. The sample $\text{Cr}_{0.51}\text{N}_{0.49}$ is close to stoichiometry (N/Me ratio = 0.96), while $\text{Cr}_{0.50}\text{V}_{0.03}\text{N}_{0.47}$ and $\text{Cr}(\text{Mo}, \text{V})\text{N}_x$ are substoichiometric with composition from $\text{Cr}_{0.50}\text{V}_{0.03}\text{N}_{0.47}$ to $\text{Cr}_{0.44}\text{Mo}_{0.09}\text{V}_{0.08}\text{N}_{0.39}$ for the lowest N-containing film. The samples $\text{Cr}_{0.51}\text{N}_{0.49}$ and $\text{Cr}_{0.50}\text{V}_{0.03}\text{N}_{0.47}$ are used as references, while the other three samples contain $\sim 8-9\%$ of Mo in the metal site and an increase in the V content from 6 to 8%. All the samples contain a negligible amount of oxygen which is less than the detection limit (~ 1 at. %) of the instrument. A plausible explanation for the higher degree of N deficiency within the $\text{Cr}(\text{Mo}, \text{V})\text{N}_x$ series compared with $\text{Cr}_{0.51}\text{N}_{0.49}$ and $\text{Cr}_{0.50}\text{V}_{0.03}\text{N}_{0.47}$ is explained below (see Sec. III B).

B. Structural analysis

1. XRD

Figure 1(a) shows θ - 2θ XRD patterns of $\text{Cr}_{0.51}\text{N}_{0.49}$, $\text{Cr}_{0.50}\text{V}_{0.03}\text{N}_{0.47}$, and $\text{Cr}(\text{Mo}, \text{V})\text{N}_x$ epitaxial thin films, described in more detail elsewhere [39]. For all samples, the (0001)-oriented Al_2O_3 substrate provides a template for twin-domain epitaxial cubic growth of the thin films along [111] direction [52]. With increase in alloying-element concentration of V and incorporation of Mo in the CrN matrix, the lattice parameter gradually decreases as evident from the shift of the 111 and 222 peaks to higher diffraction angles. Up to the highest alloying element concentration, a single-phase cubic NaCl structure is retained, with no indication of any secondary phases. The 111 peaks of each sample were fitted using pseudo-Voigt functions, and the lattice parameters determined from the 111 peak positions are listed in Table I. It can be inferred from this paper that addition of V increases the solid solubility limit of $\text{Cr}(\text{Mo}, \text{V})\text{N}_x$, preventing phase

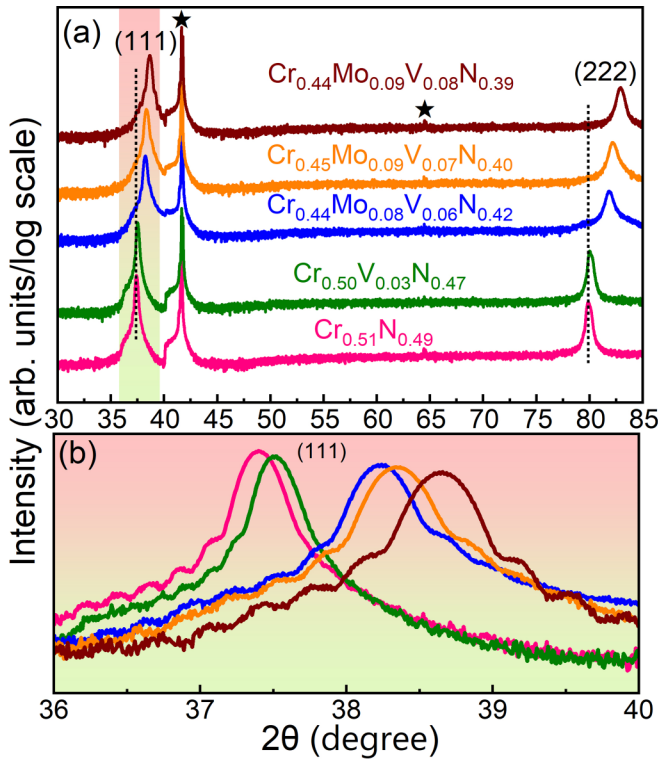


FIG. 1. (a) θ - 2θ x-ray diffraction patterns where the stars represent the corresponding substrate peaks and (b) magnified view around the 111 peak of $\text{Cr}_{0.51}\text{N}_{0.49}$, $\text{Cr}_{0.50}\text{V}_{0.03}\text{N}_{0.47}$, and $\text{Cr}(\text{Mo}, \text{V})\text{N}_x$ thin films deposited on *c*-plane (0001) sapphire substrates.

segregation of Mo_2N , as observed by Quintela *et al.* [36] in bulk $\text{Cr}_{1-x}\text{Mo}_x\text{N}$ (at $x \geq 0.025$). For $\text{Cr}_{0.51}\text{N}_{0.49}$, the lattice parameter corroborates well with literature values ~ 4.15 – 4.18 Å [52]. Note the presence of Laue oscillations [see Fig. 1(b)] in all the samples, indicating high crystallinity.

The atomic radii of Cr, V, Mo, and N are 140, 135, 145, and 65 pm, respectively. It is known that, with nitridation of Cr, phase transition from Cr (bcc) \rightarrow β - Cr_2N [hexagonal close packed (hcp)] \rightarrow CrN (rocksalt) occurs [53]. For stoichiometric CrN, the N atoms occupy 100% of the interstitial octahedral sites of the metal lattice. Earlier studies have shown alloying with V or Mo results in an increase in the lattice parameter, provided the Cr atoms are substituted by the metal atoms in bulk CrN [34,36]. Nevertheless, our RBS results confirm the presence of N vacancies in all the samples. Thus, decrease in the lattice parameter stems from the volume contraction caused by the insufficient N occupancy. Similar observations have been reported for N-deficient CrN thin films [53]. Although the metal content is considerably $>50\%$ (and N content is reduced from 47 to 39%) of the lattice site, the B1 rocksalt structure is still retained, instead of transformation to hcp Cr_2N . Within the $\text{Cr}(\text{Mo}, \text{V})\text{N}_x$ samples, the reduction in the lattice parameter follows the trend of B1 MoN_x (4.20–4.27 Å)/hcp MoN ($a = 5.72$ Å, $c = 5.60$ Å) \rightarrow fcc Mo_2N (4.16–4.19 Å) [54] with reduction in the N content. Since the lattice parameters of fcc Mo_2N and rocksalt CrN match closely, addition of Mo leads to half occupancy of N in the nonmetal site (approaching Mo_2N)

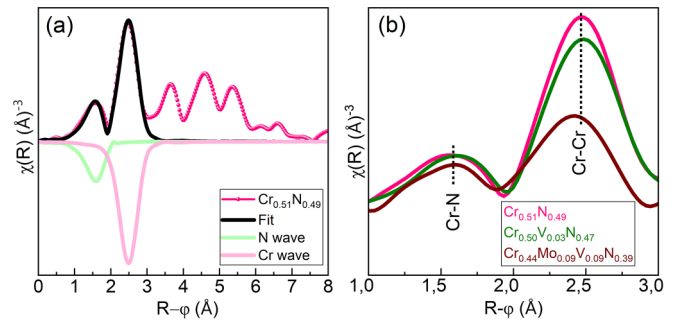


FIG. 2. (a) Fourier transform (FT) moduli $\chi(R)$ as a function of radial distribution distance ($R-\phi$) and the corresponding best fits for $\text{Cr}_{0.51}\text{N}_{0.49}$ thin film sample. (b) FT moduli in the ($R-\phi$) space for the $\text{Cr}_{0.51}\text{N}_{0.49}$, $\text{Cr}_{0.50}\text{V}_{0.03}\text{N}_{0.47}$, and $\text{Cr}_{0.44}\text{Mo}_{0.09}\text{V}_{0.08}\text{N}_{0.39}$ samples with different alloying concentrations.

resulting in more N deficiency in $\text{Cr}(\text{Mo}, \text{V})\text{N}_x$ samples compared with $\text{Cr}_{0.51}\text{N}_{0.49}$ and $\text{Cr}_{0.50}\text{V}_{0.03}\text{N}_{0.47}$.

2. EXAFS

Figure 2(a) shows the real part of the FT moduli $\chi(R)$ and the corresponding best fit as a function of radial distribution distance ($R-\phi$) for $\text{Cr}_{0.51}\text{N}_{0.49}$ thin film. The fitting of FT $\chi(R)$ of the Cr foil is shown and discussed in the Supplemental Material (Fig. S1) [42]. Single scattering theory with the first two nearest-neighbor scattering paths from the Cr absorber atom were considered for fitting the FT $\chi(R)$ spectra. The first two shells extended in 0.7–3.1 Å [see Fig. 2(a)] correlate to the Cr-N and Cr-Cr bond distances at ~ 1.55 and 2.45 Å and are consistent with the previous reports [55]. The scattering phase shift in EXAFS is typically 0.5 Å at lower ($R-\phi$) from the obtained fitted values since $\chi(k) \propto \sin(kR+\phi)$ in k space [56]. The atomic pair distances ($R_{\text{absorber-neighbor}}$) obtained from the fitting are $R_{\text{Cr-N}} = 2.08$ (± 0.04) Å and $R_{\text{Cr-Cr}} = 2.92$ (± 0.01) Å. The $R_{\text{Cr-N}}$ value is in excellent agreement, while $R_{\text{Cr-Cr}}$ is slightly at a lesser value than the XRD data ($R'_{\text{Cr-N}} = 2.079$ Å and $R'_{\text{Cr-Cr}} = 2.941$ Å). This local information may differ from the macroscopically averaged information acquired from XRD.

The fitting reveal values of $N_{\text{Cr-N}} = 4.85$ (± 1.5) and $N_{\text{Cr-Cr}} = 10.6$ (± 1.1) in the first and second coordination shell, respectively. It is to be noted that binary nitrides with rocksalt structure in octahedral symmetry are $sp^3 d^2$ hybridized. Contrary to our RBS results, from EXAFS, the N deficiency around the first coordination shell for the $\text{Cr}_{0.51}\text{N}_{0.49}$ sample cannot be stated within the error bar. Fitting of the RBS data yields an overall substoichiometry in nitrogen if the elemental distributions are assumed to be homogeneous. Local inconsistencies from the stoichiometry can be probed using EXAFS which typically extends up to 5 Å from the Cr absorber atom. EXAFS fitting further suggests locally less occupancy of Cr atoms in the second coordination shell.

Figure 2(b) shows distinct variation in the intensity of oscillations of $\text{Cr}_{0.51}\text{N}_{0.49}$, $\text{Cr}_{0.50}\text{V}_{0.03}\text{N}_{0.47}$, and highest alloyed $\text{Cr}_{0.44}\text{Mo}_{0.09}\text{V}_{0.08}\text{N}_{0.39}$ samples around the first and second coordination shell (up to 3 Å). The maximum intensity is observed at ~ 2.45 Å for $\text{Cr}_{0.51}\text{N}_{0.49}$, and it gradually decreases

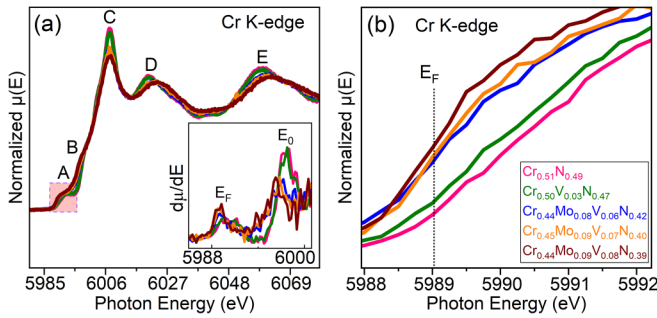


FIG. 3. (a) Normalized Cr *K*-edge x-ray absorption near-edge structure (XANES) spectra of $\text{Cr}_{0.51}\text{N}_{0.49}$, $\text{Cr}_{0.50}\text{V}_{0.03}\text{N}_{0.47}$, and $\text{Cr}(\text{Mo}, \text{V})\text{N}_x$ thin film samples in different alloying concentrations. The inset shows the first-order derivative of the absorption spectra with respect to the photon energy. E_F represents the Fermi level, and E_0 represents the absorption edge of the samples. (b) The magnified view of the same normalized Cr *K*-edge XANES spectra near the pre-edge region indicating E_F is shown for $\text{Cr}_{0.51}\text{N}_{0.49}$, $\text{Cr}_{0.50}\text{V}_{0.03}\text{N}_{0.47}$, and $\text{Cr}(\text{Mo}, \text{V})\text{N}_x$ samples.

with increasing alloying concentrations. The peak area of the radial distribution distance is correlated to the coordination number [57]. Therefore, it can be inferred that, for $\text{Cr}_{0.51}\text{N}_{0.49}$, the local coordination (N and next-nearest Cr atoms) is maximum for the Cr absorber leading to the highest intensity in both shells.

For the $\text{Cr}_{0.50}\text{V}_{0.03}\text{N}_{0.47}$ sample, the intensity of the first shell remains unaltered in comparison with $\text{Cr}_{0.51}\text{N}_{0.49}$. However, 3% alloying of V leads to substitution of few Cr atoms with V and is reflected in less Cr-Cr bonds seen from a reduced intensity around the second shell. For the $\text{Cr}_{0.44}\text{Mo}_{0.09}\text{V}_{0.08}\text{N}_{0.39}$ sample, the presence of less Cr-N and Cr-Cr bonds is evident from the radial distribution spectra compared with the rest of the samples. This is due to the bond formation of the Cr absorber atom with V and Mo atoms which substituted a few Cr atoms in the metal site. Consequently, due to substoichiometry of N as observed from our RBS results, the resultant Cr-N bonds also reduce. Locally, the less directional Cr-Cr bond length reduces for $\text{Cr}_{0.44}\text{Mo}_{0.09}\text{V}_{0.08}\text{N}_{0.39}$ compared with the rest of the samples, demonstrating a similar trend to our XRD results. This is attributed to the presence of N vacancies due to transition from covalent to metal-like character [53].

C. Electronic structure of unoccupied and occupied states

1. XANES

Figure 3(a) shows normalized Cr *K*-edge XANES spectra of $\text{Cr}_{0.51}\text{N}_{0.49}$, $\text{Cr}_{0.50}\text{V}_{0.03}\text{N}_{0.47}$, and $\text{Cr}(\text{Mo}, \text{V})\text{N}_x$ samples. The reference spectra of $\text{Cr}_{0.51}\text{N}_{0.49}$ is in line with the previous report [55]. The observed features are labeled (A)–(E). For comparison, a reference Cr foil was also measured and shown in the Supplemental Material (Fig. S2) [42]. Note that all the samples display a weak pre-edge feature, shown in Fig. 3(a) as a shaded region labeled (A). This is assigned to a single core electron excitation from the $1s$ core orbital to the unoccupied $3d$ valence states of the Cr absorber atom partially hybridized with the $2p$ valence states of the neighboring N atoms and is electric dipole allowed ($\Delta l = \pm 1$). The E_F lies around the

pre-edge, which is indicated in the inset of Fig. 3(a) [also in the magnified view of Fig. 3(b)].

Above the Fermi energy E_F , the higher-energy feature labeled (B) is attributed to $1s \rightarrow 4s$ transitions of the Cr absorber atom, with partial contribution from $2p$ - $3s$ - $3p$ states of the nitrogen ligand. This makes the electric dipole transition allowed ($\Delta l = \pm 1$) as observed for different transition metal compounds [58]. Around this region, the absorption edge (E_0) also appears [indicated in the inset of Fig. 3(a)], and the positions for all the samples are listed in Table I. The E_0 gradually shifts to the lower photon energy from $\text{Cr}_{0.51}\text{N}_{0.49}$ to $\text{Cr}_{0.44}\text{Mo}_{0.09}\text{V}_{0.08}\text{N}_{0.39}$. This is attributed to the reduced core-hole screening of the Cr ions from $\text{Cr}_{0.51}\text{N}_{0.49}$ to $\text{Cr}_{0.44}\text{Mo}_{0.09}\text{V}_{0.08}\text{N}_{0.39}$, leading to reduction in the charge transfer from Cr to N. The trend in the samples can be well corroborated to the different electronegativities of the transition elements present in the samples with 1.63 (V), 1.66 (Cr), 2.16 (Mo), and 3.04 (N) on the Pauling scale.

As seen from XRD, the samples crystallize in cubic rock-salt NaCl structure ($Fm\bar{3}m$). This structure is known to have a periodic ABCABC stacking sequence. Such a stacking sequence in the presence of a nitrogen ligand environment gives rise to an intense *white line* (a sharp intense peak in the near edge) feature labeled (C). Hence, such an observation is a fingerprint for the typical characteristics of isostructural transition metal nitrides (e.g., ScN, TiN, and VN) crystallized in the NaCl structure [59,60]. Features labeled (C) and (D) arise due to core electron transition $1s \rightarrow 4p$ obeying the electric dipole transition rule. The occupancy of electrons in the unoccupied $4p$ orbitals of the Cr absorber reflects an inverse trend in the intensity around feature (C). Feature (E) is resultant of the constructive interference of the outgoing photoelectron from the Cr absorber and backscattered photoelectron wave function from the neighboring N atoms.

A magnified view of the electronic DOS around E_F of the normalized Cr *K*-edge XANES spectra is shown in Fig. 3(b). In contrast to stoichiometric CrN [61], nonvanishing Cr $3d$ t_{2g} nonbonding and Cr $3d$ e_g antibonding states with partial contribution from N $2p$ states arise around E_F . This is due to the N-vacancy-mediated defects for substoichiometric $\text{Cr}_{0.51}\text{N}_{0.49}$ (in this paper) and is consistent with previous band structure calculations [32]. The vacancy in the N site led to occupancy of electrons back to the metallic spin-up Cr $3d$ t_{2g} nonbonding states pushing E_F inside the conduction band. The increase in the DOS around E_F with alloying [also indicated around E_F in the inset of Fig. 3(a)] is governed by the cumulative effect of alloying elements and N vacancies. The effect is strongly correlated to the change in the thermoelectric properties of the samples (discussed in Sec. III D below).

2. Soft XAS

Figure 4 shows normalized XANES spectra of Cr $L_{3,2}$, N K , Mo $M_{3,2}$, and V $L_{3,2}$ edges of $\text{Cr}_{0.51}\text{N}_{0.49}$, $\text{Cr}_{0.50}\text{V}_{0.03}\text{N}_{0.47}$, and $\text{Cr}(\text{Mo}, \text{V})\text{N}_x$ thin film samples. For $\text{Cr}_{0.51}\text{N}_{0.49}$, the doublet features (L_3 and L_2) in the Cr $L_{3,2}$ spectrum are resultant of spin-orbit splitting (ζ_{sp}) due to electric-dipole-allowed transition ($\Delta l = \pm 1$) of a core electron from Cr $2p_{3/2}$, $2p_{1/2} \rightarrow$ Cr $3d$ states owing to $\zeta_{sp} \sim 8.1$ eV. The lower energy shift of ~ 1 eV of $L_{3,2}$ peaks from the previous report suggests

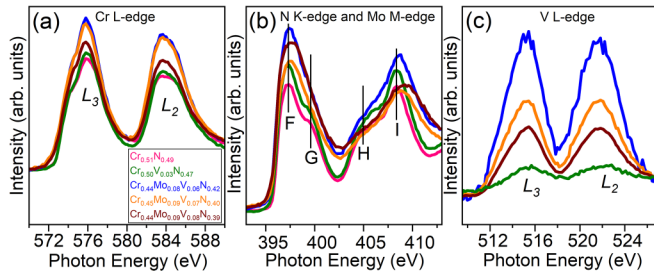


FIG. 4. (a) Normalized N K -edge and Mo $M_{3,2}$ -edge, (b) Cr $L_{3,2}$ -edge, and (c) V $L_{3,2}$ -edge x-ray absorption near-edge structure (XANES) spectra of $\text{Cr}_{0.51}\text{N}_{0.49}$, $\text{Cr}_{0.50}\text{V}_{0.03}\text{N}_{0.47}$, and $\text{Cr}(\text{Mo}, \text{V})\text{N}_x$ thin film samples with different alloying concentrations.

$\text{Cr}^{+3-\delta}$ valence state in our sample, although the line shape and ζ_{sp} value match closely with stoichiometric CrN [62]. Upon alloying, the relative changes in E_0 and ζ_{sp} values of the samples compared with $\text{Cr}_{0.51}\text{N}_{0.49}$ fall within the detection limit. Higher intensity around L_3 and L_2 for $\text{Cr}_{0.50}\text{V}_{0.03}\text{N}_{0.47}$ and $\text{Cr}(\text{Mo}, \text{V})\text{N}_x$ samples compared with $\text{Cr}_{0.51}\text{N}_{0.49}$ can be partly explained by the presence of fewer d electrons per atom of Cr upon Mo and/or V substitution, leading to higher unoccupied Cr $3d$ states.

For $\text{Cr}_{0.51}\text{N}_{0.49}$ and $\text{Cr}_{0.50}\text{V}_{0.03}\text{N}_{0.47}$ samples, four distinct features (F)–(I) in the N K edge correspond to core electron transitions from the N $1s$ core level to unoccupied hybridized states of (F) N $2p\pi + \text{Cr } 3d$, i.e., t_{2g} ; (G) N $2p\sigma + \text{Cr } 3d$, i.e., e_g ; and (H) and (I) higher unoccupied hybridized states of N $2p + \text{Cr } 4sp$. The features indicate strong hybridization between Cr $3d$ and N $2p$ states, yielding a crystal field splitting (10Dq) of ~ 2.1 eV. Usually, this parameter has significance as it is anticorrelated to the lattice parameter [i.e., $10\text{Dq} \propto (\text{bond distance})^{-5}$] and indicates hybridization strength [63]. However, no significant changes in the 10Dq values between $\text{Cr}_{0.51}\text{N}_{0.49}$ and $\text{Cr}_{0.50}\text{V}_{0.03}\text{N}_{0.47}$ are observed in this paper within the energy resolution limit. For the $\text{Cr}(\text{Mo}, \text{V})\text{N}_x$ system, an overlap between the N K edge (401.6 eV) and the Mo $M_{3,2}$ edges (spread over 392–410 eV) [64] makes it complicated to analyze the N K edge after addition of Mo. Due to the low fluorescence yield at the Mo $M_{3,2}$ edge [65], the N K edge dominates the XANES spectra. The noticeable suppression of features (G) and (H) are caused by the band smearing of unoccupied Mo $4d$ states due to the opening of the Mo $3p \rightarrow 4d$ dipole-allowed transition channel. The broadening also overshadows the relative chemical shifts of E_0 between the samples.

Like the Cr L -edge spectra, the same trend can be observed in the V L -edge spectra, where the L_3 and L_2 features start appearing for $\text{Cr}_{0.50}\text{V}_{0.03}\text{N}_{0.47}$ and become prominent for the $\text{Cr}(\text{Mo}, \text{V})\text{N}_x$ samples. However, in a simple electronic picture with higher V alloying, V should contribute with more $3d$ states. Simultaneously, more electrons should be drawn from V to N because of the lower electronegativity, provided the N content is constant. Although at a first glance it may appear simple, the presence of three transition metals with a gradual reduction of the N/Me ratio is a complex system. A smaller number of available N $2p$ states enforces the competition of the charge transfer from one of the metals to N and back

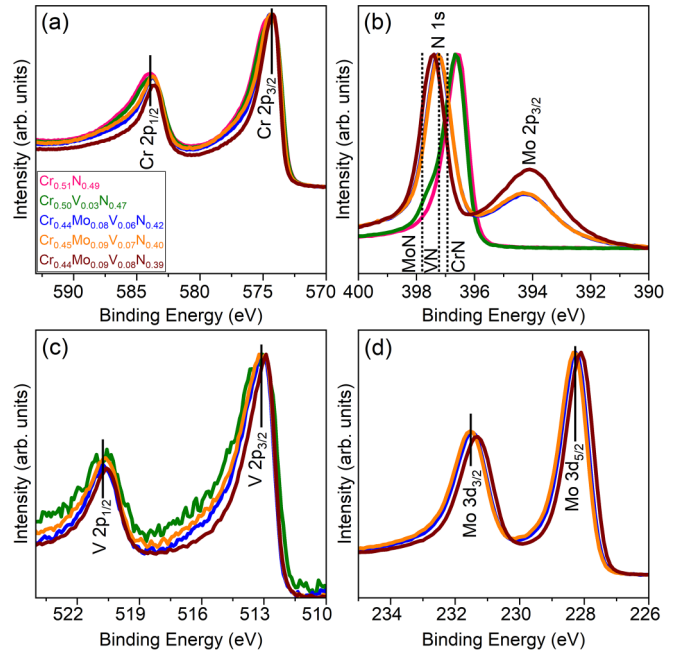


FIG. 5. X-ray photoelectron spectroscopy (XPS) core-level spectra of (a) Cr $2p$, (b) N $1s$ and Mo $2p$, (c) V $2p$, and (d) Mo $3d$ of $\text{Cr}_{0.51}\text{N}_{0.49}$, $\text{Cr}_{0.50}\text{V}_{0.03}\text{N}_{0.47}$, and $\text{Cr}(\text{Mo}, \text{V})\text{N}_x$ samples with different alloying concentrations.

to the other metal site, especially within the $\text{Cr}(\text{Mo}, \text{V})\text{N}_x$ series, depending on the electronegativities of the metals. This affects the intensity distribution, and therefore, no definite trend within the $\text{Cr}(\text{Mo}, \text{V})\text{N}_x$ system can be observed from all the absorption edges.

3. XPS

Figure 5 shows the Cr $2p$, N $1s$, Mo $2p$, V $2p$, and Mo $3d$ XPS core-level spectra normalized to the highest intensity. Cr $2p$ core-level spectra [see Fig. 5(a)] reveal the spin-split doublet peaks $2p_{3/2}$ and $2p_{1/2}$. For $\text{Cr}_{0.51}\text{N}_{0.49}$ and $\text{Cr}_{0.50}\text{V}_{0.03}\text{N}_{0.47}$, the peaks $2p_{3/2}$ and $2p_{1/2}$ are centered at ~ 574.4 and 583.9 eV. Asymmetry around the main $2p_{3/2}$ peaks is noted which arises in the Cr photoelectron spectrum owing to the multiplet structure due to unpaired electrons [66]. Around the broadened $2p_{1/2}$ peaks, this effect is less pronounced due to the Coster-Kronig effect [67]. For $\text{Cr}(\text{Mo}, \text{V})\text{N}_x$ samples, no notable peak shifts can be observed compared with $\text{Cr}_{0.51}\text{N}_{0.49}$ and $\text{Cr}_{0.50}\text{V}_{0.03}\text{N}_{0.47}$. This indicates no significant change in the valence charge distribution of Cr ions after alloying which is contrary to the observed absorption edge shift in Cr K -edge XANES spectra. Thus, the deviation can be understood in the difference of the probed volume in both the measurements. However, reduction in peak broadening and peak asymmetry can be observed with Mo and increasing V alloying concentrations.

In Fig. 5(b), the N $1s$ and Mo $2p_{3/2}$ partially overlapping peaks are shown. The dotted lines show the reference position of the N $1s$ spectra for CrN, VN, and MoN, respectively [68]. For all samples, including even $\text{Cr}_{0.51}\text{N}_{0.49}$, the N $1s$ peak shifts to lower binding energy (BE) from the reference value reported for stoichiometric CrN (396.9 eV). This is due to

the N substoichiometry (N/metal ratio is 0.96), which results in each N atom having on average more Cr neighbors. That can lead to both (i) higher negative charge density on each Cr atom and (ii) better screening of the core hole left after photoemission. Both effects result in the peak shift to lower BE. A gradual shift of the N $1s$ core-level spectra to the higher BE side can be seen for $\text{Cr}_{0.50}\text{V}_{0.03}\text{N}_{0.47}$ and $\text{Cr}(\text{Mo}, \text{V})\text{N}_x$ samples. The observation is in line with the same trend of shift from reference samples. Thus, the shift is due to gradual reduction of the N content in the nonmetal site and addition of other transition metals, i.e., Mo and V in the CrN matrix. The result implies reduction in the charge state of N. It should be noted that, in XPS, there is a probability of preferential sputtering of N during sputter cleaning of the sample surface.

V $2p$ core-level spectra shown in Fig. 5(c) reveal no significant peak shifts. The only visible change is the reduction in peak asymmetry that takes place with increasing V content. Mo $3d$ core-level spectra [see Fig. 5(d)] from $\text{Cr}_{0.44}\text{Mo}_{0.08}\text{V}_{0.06}\text{N}_{0.42}$ and $\text{Cr}_{0.45}\text{Mo}_{0.09}\text{V}_{0.07}\text{N}_{0.40}$ films are identical. A shift to the lower BE side (~ 0.2 eV) can be noted in the Mo $3d$ spectrum from the $\text{Cr}_{0.44}\text{Mo}_{0.09}\text{V}_{0.08}\text{N}_{0.39}$ sample. As the corresponding N $1s$ peak shifts to higher BE [see Fig. 5(b)], this corroborates a reduced charge transfer from the metal to the N atoms.

The ζ_{sp} values of 9.5 and 7.7 eV are obtained for Cr $2p$ and V $2p$ XPS core-level spectra. A discrepancy of 1.4 eV for Cr and 1.2 eV for V, among the ζ_{sp} values between the XAS and XPS measurements can be noted. This is due to excitation of the electrons to different final states involved in both processes. Considering $2p^6 3d^n$ as the ground state, the final states for XAS and XPS are $2p^5 3d^{n+1}$ and $2p^6 3d^n$, respectively. It leads to variable exchange and Coulomb interaction between the transition states involved, resulting in such a discrepancy [69]. The theoretical total DOS calculations (Figs. S3(a), S3(c), and S3(e) in the Supplemental Material [42]) reveal contribution from the different states in the valence band spectra.

4. VBS

Figure 6 shows valence band spectra for the $\text{Cr}_{0.51}\text{N}_{0.49}$, $\text{Cr}_{0.50}\text{V}_{0.03}\text{N}_{0.47}$, and the $\text{Cr}(\text{Mo}, \text{V})\text{N}_x$ samples with their indicated E_F . The theoretical total DOS calculations are shown in Fig. S3 in the Supplemental Material [42]. Note that double-layer antiferromagnetic ordering with a Hubbard parameter $U = 3$ was considered in the calculations [70]. The calculations were used to identify the hybridization contributions and their positions in the valence band spectra.

In contrast to stoichiometric CrN known to exhibit a narrow band gap [61,71], finite DOS around E_F in this paper is attributed to the presence of N vacancies in the $\text{Cr}_{0.51}\text{N}_{0.49}$ thin film sample. From previous studies, it is known theoretically that N vacancies induce n -type behavior in the DOS [32]. However, in this paper, the x-ray width is ~ 0.3 eV. Feature (Q) arises mainly due to the contribution from the Cr $3d$ states hybridized with N $2p$ states, whereas feature (R) ~ 5 –8 eV is an effect from Cr $3d$ states hybridized to N $2p$ states with partial contribution from Cr $3p$ states. The shoulder (at 6.5 eV) arises as intense as the main feature (R) (5.2 eV) and appears as a doublet [72]. The contribution of feature (S) is mostly

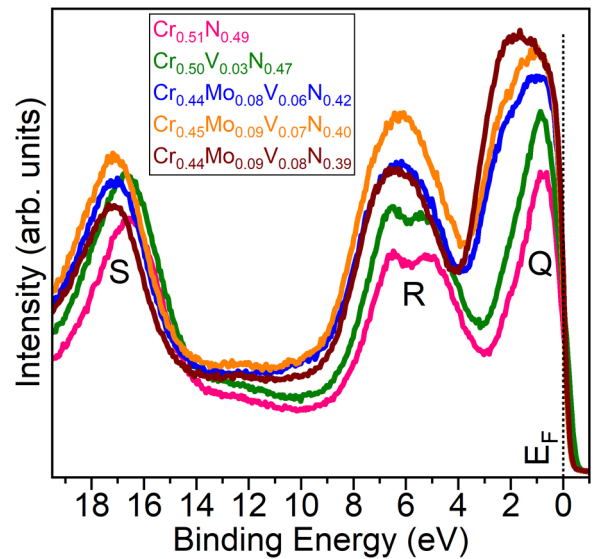


FIG. 6. Valence band spectra of $\text{Cr}_{0.51}\text{N}_{0.49}$, $\text{Cr}_{0.50}\text{V}_{0.03}\text{N}_{0.47}$, and $\text{Cr}(\text{Mo}, \text{V})\text{N}_x$ samples with different alloying concentrations.

dominated by N $2s$ states with a small contribution from Cr $3d$ states.

For the $\text{Cr}_{0.50}\text{V}_{0.03}\text{N}_{0.47}$ sample, the features of the valence band spectra reciprocate a similar trend to $\text{Cr}_{0.51}\text{N}_{0.49}$. However, calculated total DOS reveals essential contribution from both Cr $3d$ and N $2p$ states with partial contribution from V $3d$ states for feature (Q) in this sample [35]. Feature (R) unveils hybridization of N $2p$ states with (Cr,V) $3d$ and small contribution from Cr $3p$ states. Feature (S) is dominated by hybridization of N $2s$ states with marginal contribution from Cr $3d$ states.

For $\text{Cr}(\text{Mo}, \text{V})\text{N}_x$ samples, the main contribution of the features is due to the hybridization of the following states:

- (1) Feature (Q) at ~ 0.8 – 1.6 eV: N $2p$ states—Cr $3d$, V $3d$, and primarily Mo $4d$ states.
- (2) Feature (R) ~ 5 – 8 eV: N $2p$ states—Cr ($3d$, $3p$)/V ($3d$, $3p$)/Mo $4d$ states.
- (3) Feature (S) ~ 16 eV: N $2s$ states—small contribution from Cr ($3p$, $3d$)/Mo $4d$ states.

Here, a band smearing across feature (Q) is due to overlap of the broadened $4d$ wave functions of Mo with (Cr,V) $3d$ wave functions leading to delocalization of the valence band. The effect is also pronounced around feature (R) with a diminished doublet feature as was observed for $\text{Cr}_{0.51}\text{N}_{0.49}$ and $\text{Cr}_{0.50}\text{V}_{0.03}\text{N}_{0.47}$. For feature (S), a shift to lower BE (0.5 eV) can be observed for $\text{Cr}(\text{Mo}, \text{V})\text{N}_x$ samples compared with $\text{Cr}_{0.51}\text{N}_{0.49}$ and $\text{Cr}_{0.50}\text{V}_{0.03}\text{N}_{0.47}$.

5. RIXS

Figure 7(a) shows Cr $2p$ RIXS and Cr $L_{3,2}$ -edge XAS data, and Fig. 7(b) shows N $1s$ RIXS and N K -edge XAS data, respectively, of the $\text{Cr}_{0.51}\text{N}_{0.49}$, $\text{Cr}_{0.50}\text{V}_{0.03}\text{N}_{0.47}$, and the $\text{Cr}(\text{Mo}, \text{V})\text{N}_x$ thin film samples. The peak maxima in the XAS data were used to determine the photon energies for the emission measurements. Cr $2p$ RIXS on a Cr thin metal film is shown in the Supplemental Material (Fig. S4) [42] to obtain insight on the p-DOS and a comparison between Cr and

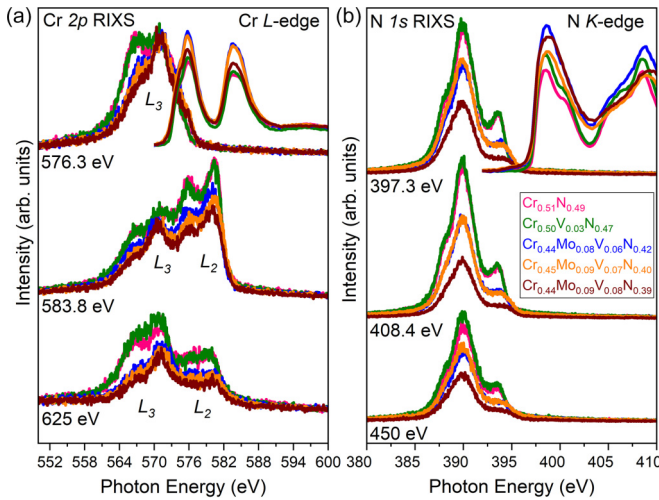


FIG. 7. (a) Cr $2p$ resonant inelastic x-ray scattering (RIXS) at different excitation photon energies of 576.3 eV (resonant), 583.8 eV (resonant), and 625 eV (nonresonant), respectively, and Cr $L_{3,2}$ -edge x-ray absorption (XAS) data (top right). (b) N $1s$ RIXS at different excitation photon energies of 397.3 eV (resonant), 408.4 eV (resonant), and 450 eV (nonresonant), respectively, and N K -edge XAS of the Cr_{0.51}N_{0.49}, Cr_{0.50}V_{0.03}N_{0.47}, and the Cr(Mo, V)N_x thin film samples.

Cr_{0.51}N_{0.49}. The Cr $2p$ RIXS spectra represents the sd -DOS of the occupied Cr states of the valence band following the Cr $3d4s \rightarrow 2p_{3/2,1/2}$ dipole transitions ($\Delta l = \pm 1$).

The spectra excited at 576.3 eV (resonant) show doublet features in the valence band region. In contrast, the spectra excited at 583.8 eV (resonant) and 625 eV (nonresonant) exhibit four features. For all samples, we attribute these features in the valence band region as L_3 and L_2 emission with a t_{2g} - e_g subsplitting. The most intense L_3 emission at 576.3 eV and L_2 emission at 583.8 eV are due to excitation at the $2p_{3/2}$ and $2p_{1/2}$ absorption edges. The feature at the lowest emission energy arises primarily due to $3d t_{2g}$ orbitals, with partial N $2p$ contribution, whereas at higher emission energy, the $3d e_g$ orbitals with admixture of N $2p$ orbitals dominate [70,73].

At 576.3 eV excitation energy, the relatively large distance of the band maxima from the crossover of the RIXS and XAS spectra of this band region is an indication of strong covalent bonding between Cr and N. However, the doublet feature is less pronounced for the Cr(Mo, V)N_x samples with reduced bandwidth. It indicates a decrease in the Cr $3d$ -N $2p$ hybridization, with reduced states leading to less covalent bonds. For 583.8 eV excitation energy, a reduced intensity of the Cr(Mo, V)N_x samples is observed compared with the Cr_{0.51}N_{0.49} and Cr_{0.50}V_{0.03}N_{0.47} samples, in line with the reduced atomic percent of Cr from our RBS measurements (see Table I). At nonresonant 625 eV excitation energy, the L_3/L_2 branching ratio increases from 1.9 for Cr_{0.51}N_{0.49} to 4.4 for Cr_{0.44}Mo_{0.09}V_{0.08}N_{0.39}. Quantitatively, the significantly higher L_3/L_2 ratio for the Cr_{0.44}Mo_{0.09}V_{0.08}N_{0.39} sample compared with the statistical ratio (2:1) is due to the more effective Coster-Kronig process in conducting systems compared with more localized electrons with less conduction of the Cr_{0.51}N_{0.49} sample [74].

The N $1s$ RIXS spectra representing the p -DOS of the N valence region follows the $2p \rightarrow 1s$ dipole transitions. The N $1s$ RIXS spectra excited for all the samples at resonant photon energy of 397.3 eV exhibits a main peak centered ~ 389.9 eV composed of primarily N $2p$ states, in agreement with band structure calculations [75]. We interpret the low-energy emission shoulder at ~ 388 eV below the main peak as N $2s$ - $2p$ hybridization. A higher-energy shoulder at ~ 393.6 eV is also observed attributed to N $2p$ states hybridized with Cr $3d$ states, in line with theoretical density functional theory calculations [61]. The intensity of this shoulder is highest for the Cr_{0.51}N_{0.49} and Cr_{0.50}V_{0.03}N_{0.47} samples due to more directional bonds and more charge withdrawal from Cr and V to N when there is no Mo content. For the Cr(Mo, V)N_x samples containing Mo, the number of hybridized N $2p$ states around the crossover region are significantly higher. This in turn affects the electrical resistivity within the samples, as discussed in the next section. Contrary to the Cr $2p$ RIXS, most excitation-energy-dependent changes in the N $1s$ RIXS are only observed in the high-energy shoulder, while there are only minor changes in the main peak. This is a signature of delocalized N $2p$ states compared with the more localized Cr $3d$ states.

D. Seebeck coefficient and electrical resistivity

The Seebeck coefficient and electrical resistivity (ρ) of Cr_{0.51}N_{0.49}, Cr_{0.50}V_{0.03}N_{0.47}, and Cr(Mo, V)N_x samples are tabulated in Table II. For the Seebeck coefficient, Eq. (1) can be rewritten as [76]

$$S = \frac{8\pi^2 k_B^2 T}{3qh^2} m^* \left(\frac{\pi}{3n}\right)^{2/3}. \quad (4)$$

Combining Eqs. (4) and (2), the Seebeck coefficient and electrical conductivity are interrelated. For Cr_{0.51}N_{0.49}, the presence of a small amount of N vacancies results in an S value of $-93 \mu\text{V K}^{-1}$ at room temperature which is at least three times higher than earlier reports without any postdeposition treatment [17,52]. Rather, ρ and the thermoelectric power factor $S^2\sigma$ value also seem to be at par with stoichiometric bulk CrN [77]. Based on Mahan-Sofa theory, enhanced thermoelectricity is correlated with a narrow electronic energy distribution near E_F [30]. We attribute the enhanced properties for Cr_{0.51}N_{0.49} to the presence of sharp and local increase in the DOS near E_F , as observed in VBS spectra [see feature (Q) in Fig. 6]. This observation is in line with the estimated theoretical band structure calculations [21]. Moreover, in a simplified picture combining Eqs. (2) and (3), the electrical conductivity ($\propto 1/\rho$) is proportional to DOS at E_F if the electronic scattering is independent of energy [22]. In this paper, since all measurements were done at room temperature, the following picture can be considered. For Cr_{0.50}V_{0.03}N_{0.47}, S remains nearly the same, but the abrupt decrease in the ρ value is correlated to the increased population across E_F , as observed from Cr K -edge XANES spectra [see the DOS around E_F in Fig. 3(b)] resulting in a value six times higher in power factor compared with Cr_{0.51}N_{0.49}. The lower N content compared with Cr_{0.51}N_{0.49} and the lowest alloying of V lead to lower hybridization of the Cr $3d$ -N $2p$ states, as

TABLE II. The Seebeck coefficient, electrical resistivity, and power factor of the samples.

Samples	S ($\mu\text{V K}^{-1}$)	ρ ($\mu\Omega\text{ cm}$)	$S^2\sigma \pm 25\%$ ($\mu\text{W cm}^{-1}\text{ K}^{-2}$)
$\text{Cr}_{0.51}\text{N}_{0.49}$	-93 ± 1.0	26722 ± 2820	0.3
$\text{Cr}_{0.50}\text{V}_{0.03}\text{N}_{0.47}$	-95 ± 0.9	4460 ± 1000	2
$\text{Cr}_{0.44}\text{Mo}_{0.08}\text{V}_{0.06}\text{N}_{0.42}$	-14 ± 0.6	314 ± 3	0.6
$\text{Cr}_{0.45}\text{Mo}_{0.09}\text{V}_{0.07}\text{N}_{0.40}$	-9 ± 0.3	253 ± 2	0.3
$\text{Cr}_{0.44}\text{Mo}_{0.09}\text{V}_{0.08}\text{N}_{0.39}$	-7 ± 0.4	192 ± 5	0.2

observed from the contribution around feature (Q) in VBS spectra, revealing lower ρ without altering S . However, for the $\text{Cr}(\text{Mo}, \text{V})\text{N}_x$ series, a large reduction in ρ with typical metal-like S values originates from the strong hybridization of the N $2p$ - (Cr, V) $3d$ states with Mo $4d$ states (hybridization contribution as discussed in VBS spectra of Sec. III C) inducing higher DOS across E_F , as evidenced from our Cr K -edge XANES [see the DOS around E_F in Fig. 3(b)]. The crossover of significant DOS around E_F results in metal-like resistivity. Moreover, a strong coupling between Mo $4d$ and N $2p$ states near the Fermi level weakens the Cr $3d$ -N $2p$ electronic correlations for $\text{Cr}(\text{Mo}, \text{V})\text{N}_x$, driving it far from a Mott insulator [36]. The reduced S of $\text{Cr}(\text{Mo}, \text{V})\text{N}_x$ stems from the presence of broadened Mo $4d$ wave functions, inducing delocalization which drives it away from sharp and local increase in the DOS near E_F compared with $\text{Cr}_{0.51}\text{N}_{0.49}$ and $\text{Cr}_{0.50}\text{V}_{0.03}\text{N}_{0.47}$. However, the power factor of $\text{Cr}(\text{Mo}, \text{V})\text{N}_x$ series is still comparable with $\text{Cr}_{0.51}\text{N}_{0.49}$ which we attribute to the N substoichiometry. The obtained power factors of $\text{Cr}(\text{Mo}, \text{V})\text{N}_x$ samples at room temperature are typically an order of magnitude less than the conventional thermoelectric materials ScN , PbTe , and Bi_2Te_3 [22,78,79]. We attribute it to the low thickness of the samples, high N substoichiometry, and high alloying concentrations of Mo and V in CrN.

IV. CONCLUSIONS

In summary, we systematically studied the effect of V and/or Mo alloying in the CrN matrix, with substoichiometric N. The addition of V stabilizes the cubic phase retention in this complex system despite the presence of higher atomic percent of Mo. Even a small N substoichiometry led to decreased band gap in $\text{Cr}_{0.51}\text{N}_{0.49}$. This is due to fewer N $2p$ states available to accommodate the electrons, and thus, the electrons return to the metal site, shifting the Fermi level toward the conduction band. For $\text{Cr}_{0.50}\text{V}_{0.03}\text{N}_{0.47}$, less N content and the lowest amount of V alloying lead to lower hybridization of the Cr $3d$ -N $2p$ states, revealing lower electrical resistivity without altering the Seebeck coefficient. This results in overall improvement of the thermoelectric power factor. Hence, it can be inferred that presence of N deficiency up to a critical limit still retains good thermoelectric properties. Later, in the $\text{Cr}(\text{Mo}, \text{V})\text{N}_x$ series, the combined effect of N substoichiometry and contribution of Mo $4d$ hybridized to N $2p$ states weakens the Cr $3d$ -N $2p$ electronic correlations, driving it far from a Mott insulator. It is governed by crossover of significant DOS across the Fermi level compared with

$\text{Cr}_{0.51}\text{N}_{0.49}$ and $\text{Cr}_{0.50}\text{V}_{0.03}\text{N}_{0.47}$, exhibiting metal-like resistivity. The increased N substoichiometry for $\text{Cr}(\text{Mo}, \text{V})\text{N}_x$ also leads to a reduction in the charge transfer from metal to N site compared with $\text{Cr}_{0.51}\text{N}_{0.49}$. The reduced Seebeck coefficient of $\text{Cr}(\text{Mo}, \text{V})\text{N}_x$ stems from the presence of broadened Mo $4d$ wave functions which drive it away from sharp and local increase in the DOS just below the Fermi level. Thus, in this paper, we show the potential of $\text{Cr}(\text{Mo}, \text{V})\text{N}_x$ as a thermoelectric material which is strongly correlated to the DOS present near the Fermi level. This paper motivates further research on N-stoichiometric $\text{Cr}(\text{Mo}, \text{V})\text{N}$ with lower alloying concentration of Mo for enhancement of the thermoelectric properties.

ACKNOWLEDGMENTS

The authors acknowledge funding from the Swedish Government Strategic Research Area in Materials Science on Functional Materials at Linköping University (Faculty Grant SFO-Mat-LiU No. 2009 00971), the Knut and Alice Wallenberg Foundation through the Wallenberg Academy Fellows program (No. KAW-2020.0196), the Swedish Research Council (VR) under Project No. 2021-03826. M.M. also acknowledges financial support from the Swedish Energy Agency (Grant No. 43606-1) and the Carl Tryggers Foundation (No. CTS20:272, No. CTS16:303, and No. CTS14:310). R.S. acknowledges support from the Swedish Research Council VR International Postdoc Grant No. 2022-00213 and the IUVSTA through the Medard W. Welch International Scholarship 2022. G.G. acknowledges the Swedish Energy Agency Project No. 51201-1, the Åforsk Foundation Grant No. 22-4, and the Olle Engqvist Foundation Grant No. 222-0053. Research conducted at MAX IV, a Swedish national user facility, is supported by the Swedish Research council under Contract No. 2018-07152, the Swedish Governmental Agency for Innovation Systems (VINNOVA) under Contract No. 2018-04969, and Formas under Contract No. 2019-02496. The FEFF calculations were enabled by resources provided by the National Academic Infrastructure for Supercomputing in Sweden at Linköping University funded by the Swedish Research Council through Grant Agreement No. 2022-06725. Daniel Primetzhofer from Uppsala University is acknowledged for accelerator operation supported by the Swedish Research Council VR-RFI (Contract No. 2019-00191) and the Swedish Foundation for Strategic Research (Contract No. RIF14-0053).

- [1] P. Eklund, S. Kerdsonpanya, and B. Alling, Transition-metal-nitride-based thin films as novel energy harvesting materials, *J. Mater. Chem. C* **4**, 3905 (2016).
- [2] A. Filippetti and N. A. Hill, Magnetic stress as a driving force of structural distortions: The case of CrN, *Phys. Rev. Lett.* **85**, 5166 (2000).
- [3] K. Alam, S. M. Disseler, W. D. Ratcliff, J. A. Borchers, R. Ponce-Pérez, G. H. Coccoletzi, N. Takeuchi, A. Foley, A. Richard, D. C. Ingram *et al.*, Structural and magnetic phase transitions in chromium nitride thin films grown by rf nitrogen plasma molecular beam epitaxy, *Phys. Rev. B* **96**, 104433 (2017).
- [4] C. Constantin, M. B. Haider, D. Ingram, and A. R. Smith, Metal/semiconductor phase transition in chromium nitride(001) grown by rf-plasma-assisted molecular-beam epitaxy, *Appl. Phys. Lett.* **85**, 6371 (2004).
- [5] B. Biswas, S. Chakraborty, A. Joseph, S. Acharya, A. I. K. Pillai, C. Narayana, V. Bhatia, M. Garbrecht, and B. Saha, Secondary phase limited metal-insulator phase transition in chromium nitride thin films, *Acta Mater.* **227**, 117737 (2022).
- [6] Q. Jin, J. Zhao, and M. A. Roldan, Anisotropic electronic phase transition in CrN epitaxial thin films, *Appl. Phys. Lett.* **120**, 73103 (2022).
- [7] P. H. Mayrhofer, C. Mitterer, L. Hultman, and H. Clemens, Microstructural design of hard coatings, *Prog. Mater. Sci.* **51**, 1032 (2006).
- [8] Z. Wan, T. F. Zhang, H.-B.-R. Lee, J. H. Yang, W. C. Choi, B. Han, K. H. Kim, and S.-H. Kwon, Improved corrosion resistance and mechanical properties of CrN hard coatings with an atomic layer deposited Al₂O₃ interlayer, *ACS Appl. Mater. Interfaces* **7**, 26716 (2015).
- [9] W. Ecker, J. Keckes, M. Krobath, J. Zalesak, R. Daniel, M. Rosenthal, and J. Todt, Nanoscale evolution of stress concentrations and crack morphology in multilayered CrN coating during indentation: Experiment and simulation, *Mater. Des.* **188**, 108478 (2020).
- [10] D. A. Wright, Thermoelectric properties of bismuth telluride and its alloys, *Nature (London)* **181**, 834 (1958).
- [11] Z. H. Zheng, X.-L. Shi, D.-W. Ao, W.-D. Liu, M. Li, L.-Z. Kou, Y.-X. Chen, F. Li, M. Wei, G.-X. Liang *et al.*, Harvesting waste heat with flexible Bi₂Te₃ thermoelectric thin film, *Nat. Sustain.* **6**, 180 (2023).
- [12] H. Kleinke, New bulk materials for thermoelectric power generation: Clathrates and complex antimonides, *Chem. Mater.* **22**, 604 (2010).
- [13] C. B. Vining, An inconvenient truth about thermoelectrics, *Nat. Mater.* **8**, 83 (2009).
- [14] R. Amatya and R. J. Ram, Trend for thermoelectric materials and their earth abundance, *J. Electron. Mater.* **41**, 1011 (2012).
- [15] B. Biswas and B. Saha, Development of semiconducting ScN, *Phys. Rev. Mater.* **3**, 020301 (2019).
- [16] A. S. Botana, V. Pardo, and W. E. Pickett, All-3d electron-hole bilayers in CrN/MgO (111) multilayers for thermoelectric applications, *Phys. Rev. Appl.* **7**, 024002 (2017).
- [17] C. X. Quintela, J. P. Podkaminer, M. N. Luckyanova, T. R. Paudel, E. L. Thies, D. A. Hillsberry, D. A. Tenne, E. Y. Tsymlal, G. Chen, C.-B. Eom *et al.*, Epitaxial CrN thin films with high thermoelectric figure of merit, *Adv. Mater.* **27**, 3032 (2015).
- [18] I. Stockem, A. Bergman, A. Glensk, T. Hickel, F. Körmann, B. Grabowski, J. Neugebauer, and B. Alling, Anomalous phonon lifetime shortening in paramagnetic CrN caused by spin-lattice coupling: A combined spin and *ab initio* molecular dynamics study, *Phys. Rev. Lett.* **121**, 125902 (2018).
- [19] J. R. Sootsman, H. Kong, C. Uher, J. J. D'Angelo, C.-I. Wu, T. P. Hogan, T. Caillat, and M. G. Kanatzidis, Large enhancements in the thermoelectric power factor of bulk PbTe at high temperature by synergistic nanostructuring, *Angew. Chem.* **120**, 8746 (2008).
- [20] M. S. Dresselhaus, G. Chen, M. Y. Tang, R. Yang, H. Lee, D. Wang, Z. Ren, J. P. Fleurial, and P. Gogna, New directions for low-dimensional thermoelectric materials, *Adv. Mater.* **19**, 1043 (2007).
- [21] J. P. Heremans, V. Jovovic, E. S. Toberer, A. Saramat, K. Kurosaki, A. Charoenphakdee, S. Yamanaka, and G. J. Snyder, Enhancement of thermoelectric of the electronic density of states, *Science* **321**, 554 (2008).
- [22] J. R. Sootsman, D. Y. Chung, and M. G. Kanatzidis, New and old concepts in thermoelectric materials, *Angew. Chem. Int. Ed.* **48**, 8616 (2009).
- [23] C. J. Vineis, A. Shakouri, A. Majumdar, and M. G. Kanatzidis, Nanostructured thermoelectrics: Big efficiency gains from small features, *Adv. Mater.* **22**, 3970 (2010).
- [24] Z. Chen, B. Ge, W. Li, S. Lin, J. Shen, Y. Chang, R. Hanus, G. J. Snyder, and Y. Pei, Vacancy-induced dislocations within grains for high-performance PbSe thermoelectrics, *Nat. Commun.* **8**, 13828 (2017).
- [25] M. Wu, H.-H. Cui, S. Cai, S. Hao, Y. Liu, T. P. Bailey, Y. Zhang, Z. Chen, Y. Luo, C. Uher *et al.*, Weak electron-phonon coupling and enhanced thermoelectric performance in *n*-type PbTe-Cu₂Se via dynamic phase conversion, *Adv. Energy Mater.* **13**, 2203325 (2023).
- [26] N. Tureson, M. Marteau, T. Cabioch, N. V. Nong, J. Jensen, J. Lu, G. Greczynski, D. Fournier, N. Singh, A. Soni *et al.*, Effect of ion-implantation-induced defects and Mg dopants on the thermoelectric properties of ScN, *Phys. Rev. B* **98**, 205307 (2018).
- [27] P. Hones, R. Sanjinés, and F. Lévy, Sputter deposited chromium nitride based ternary compounds for hard coatings, *Thin Solid Films* **332**, 240 (1998).
- [28] H. Lind, R. Forsé, B. Alling, N. Ghafoor, F. Tasná Di, M. P. Johansson, I. A. Abrikosov, and M. Odén, Improving thermal stability of hard coating films via a concept of multicomponent alloying, *Appl. Phys. Lett.* **99**, 091903 (2011).
- [29] S. Kerdsonpanya, B. Sun, and F. Eriksson, Experimental and theoretical investigation of Cr_{1-x}Sc_xN solid solutions for thermoelectrics, *J. Appl. Phys.* **120**, 215103 (2016).
- [30] G. D. Mahan and J. O. Sofo, The best thermoelectric, *Proc. Natl. Acad. Sci. USA* **93**, 7436 (1996).
- [31] S. Kerdsonpanya, B. Alling, and P. Eklund, Effect of point defects on the electronic density of states of ScN studied by first-principles calculations and implications for thermoelectric properties, *Phys. Rev. B* **86**, 195140 (2012).
- [32] E. Mozafari, B. Alling, P. Steneteg, and I. A. Abrikosov, Role of N defects in paramagnetic CrN at finite temperatures from first principles, *Phys. Rev. B* **91**, 094101 (2015).
- [33] L. Zhou, F. Körmann, D. Holec, M. Bartosik, B. Grabowski, J. Neugebauer, and P. H. Mayrhofer, Structural stability and

- thermodynamics of CrN magnetic phases from ab initio calculations and experiment, *Phys. Rev. B* **90**, 184102 (2014).
- [34] C. X. Quintela, F. Rivadulla, and J. Rivas, Electronic and magnetic phase diagram of $\text{Cr}_{1-x}\text{V}_x\text{N}$, *Phys. Rev. B* **82**, 245201 (2010).
- [35] M. A. Gharavi, D. Gambino, A. le Febvrier, F. Eriksson, R. Armiento, B. Alling, and P. Eklund, High thermoelectric power factor of pure and vanadium-alloyed chromium nitride thin films, *Mater. Today Commun.* **28**, 102493 (2021).
- [36] C. X. Quintela, B. Rodríguez-González, and F. Rivadulla, Thermoelectric properties of heavy-element doped CrN, *Appl. Phys. Lett.* **104**, 022103 (2014).
- [37] L. J. P. Ament, M. van Veenendaal, T. P. Devereaux, J. P. Hill, and J. van den Brink, Resonant inelastic x-ray scattering studies of elementary excitations, *Rev. Mod. Phys.* **83**, 705 (2011).
- [38] A. Le Febvrier, L. Landälv, T. Liersch, D. Sandmark, P. Sandström, and P. Eklund, An upgraded ultra-high vacuum magnetron-sputtering system for high-versatility and software-controlled deposition, *Vacuum* **187**, 110137 (2021).
- [39] V. Hjort, N. K. Singh, S. Chowdhury, R. Shu, A. Le Febvrier, and P. Eklund, Phase composition and thermoelectric properties of epitaxial CrMoVN thin films, *Adv. Energy Sustain. Res.* **2023**, 2300119 (2023).
- [40] M. Mayer, S. Möller, M. Rubel, A. Widdowson, S. Charisopoulos, T. Ahlgren, E. Alves, G. Apostolopoulos, N. P. Barradas, S. Donnelly *et al.*, Ion beam analysis of fusion plasma-facing materials and components: Facilities and research challenges, *Nucl. Fusion*. **60**, 025001 (2020).
- [41] M. Mayer, SIMNRA User's Guide (Max-Planck-Institute für Plasmaphysik, Garching, 1997).
- [42] See Supplemental Material at <http://link.aps.org/supplemental/10.1103/PhysRevB.108.205134> for describing the compositional analysis by ERDA, thickness and mass density by XRR of $\text{Cr}_{0.51}\text{N}_{0.49}$, $\text{Cr}_{0.50}\text{V}_{0.03}\text{N}_{0.47}$ and $\text{Cr}(\text{Mo}, \text{V})\text{N}_x$ thin film samples. The theoretical DOS calculations of CrN, CrVN and Cr(Mo, V)N is discussed. A comparison of EXAFS, Cr *K*-edge XANES and RIXS between Cr foil and $\text{Cr}_{0.51}\text{N}_{0.49}$ is also discussed.
- [43] J. Nordgren and R. Nyholm, Design of a portable large spectral range grazing incidence instrument, *Nucl. Instrum. Methods Phys. Res. A* **246**, 242 (1986).
- [44] J. Nordgren, G. Bray, S. Cramm, R. Nyholm, J.-E. Rubensson, and N. Wassdahl, Soft x-ray emission spectroscopy using monochromatized synchrotron radiation (invited), *Rev. Sci. Instrum.* **60**, 1690 (1989).
- [45] M. Magnuson, N. Wassdahl, and J. Nordgren, Energy dependence of Cu satellites using synchrotron excited x-ray-emission spectroscopy, *Phys. Rev. B* **56**, 12238 (1997).
- [46] K. Klementiev, K. Norén, S. Carlson, K. G. V. Sigfridsson Clauss, and I. Persson, The BALDER Beamline at the MAX IV Laboratory, *J. Phys. Conf. Ser.* **712**, 012023 (2016).
- [47] J. J. Rehr, J. J. Kas, M. P. Prange, A. P. Sorini, Y. Takimoto, and F. Vila, *Ab initio* theory and calculations of x-ray spectra, *Comptes Rendus Phys.* **10**, 548 (2009).
- [48] J. J. Rehr, J. J. Kas, F. D. Vila, M. P. Prange, and K. Jorissen, Parameter-free calculations of x-ray spectra with FEFF9, *Phys. Chem. Chem. Phys.* **12**, 5503 (2010).
- [49] K. V. Klementev, Extraction of the fine structure from x-ray absorption spectra, *J. Phys. D: Appl. Phys.* **34**, 209 (2001).
- [50] I. Miccoli, F. Edler, H. Pfnür, and C. Tegenkamp, The 100th anniversary of the four-point probe technique: The role of probe geometries in isotropic and anisotropic systems, *J. Phys. Condens. Matter* **27**, 223201 (2015).
- [51] B. Xin, A. Le Febvrier, L. Wang, N. Solin, B. Paul, and P. Eklund, Growth and optical properties of Ca_xCoO_2 thin films, *Mater. Des.* **210**, 110033 (2021).
- [52] A. Le Febvrier, D. Gambino, F. Giovannelli, B. Bakhit, S. Hurand, G. Abadias, B. Alling, and P. Eklund, *p*-type behavior of CrN thin films via control of point defects, *Phys. Rev. B* **105**, 104108 (2022).
- [53] Z. Zhang, H. Li, R. Daniel, C. Mitterer, and G. Dehm, Insights into the atomic and electronic structure triggered by ordered nitrogen vacancies in CrN, *Phys. Rev. B* **87**, 014104 (2013).
- [54] H. Ihara, Y. Kimura, K. Senzaki, H. Kezuka, and M. Hirabayashi, Electronic structures of B1 MoN, fcc Mo_2N , and hexagonal MoN, *Phys. Rev. B* **31**, 3177 (1985).
- [55] Y. Tripathi, R. Gupta, Seema M. Gupta, D. M. Phase, and P. Rajput, Study of phase formulation in CrN thin films and its response to a minuscule oxygen flow in reactive sputtering process, *Thin. Solid. Films* **670**, 113 (2019).
- [56] P. A. O'Day, J. J. Rehr, S. I. Zabinsky, and G. E. Brown, Extended x-ray absorption fine structure (EXAFS) analysis of disorder and multiple-scattering in complex crystalline solids, *J. Am. Chem. Soc.* **116**, 2938 (1994).
- [57] K. W. Chapman, Emerging operando and x-ray pair distribution function methods for energy materials development, *MRS Bull.* **41**, 231 (2016).
- [58] V. Moisy-Maurice and C. H. de Novion, An application of Ti-K x-ray absorption edges and fine structures to the study of substoichiometric titanium carbide TiC_{1-x} , *J. Phys.* **49**, 1737 (1988).
- [59] S. Chowdhury, R. Gupta, P. Rajput, A. Tayal, D. Rao, R. Sekhar, S. Prakash, R. Rajagopalan, S. N. Jha, B. Saha *et al.*, Detailed study of reactively sputtered ScN thin films at room temperature, *Materialia* **22**, 101375 (2022).
- [60] C. Shang, G. Li, B. Wei, J. Wang, R. Gao, Y. Tian, Q. Chen, Y. Zhang, L. Shui, G. Zhou *et al.*, Dissolving vanadium into titanium nitride lattice framework for rational polysulfide regulation in Li-S batteries, *Adv. Energy Mater.* **11**, 2003020 (2021).
- [61] T. Cheiwchanchamnangij and W. R. L. Lambrecht, Quasiparticle self-consistent *GW* band structure of CrN, *Phys. Rev. B* **101**, 085103 (2020).
- [62] Q. Jin, H. Cheng, Z. Wang, Q. Zhang, S. Lin, M. A. Roldan, J. Zhao, J.-O. Wang, S. Chen, M. He *et al.*, Strain-mediated high conductivity in ultrathin antiferromagnetic metallic nitrides, *Adv. Mater.* **33**, 2005920 (2021).
- [63] K. Knížek, P. Novák, and Z. Jiráček, Spin state of LaCoO_3 : Dependence on CoO_6 octahedra geometry, *Phys. Rev. B* **71**, 054420 (2005).
- [64] W. Zheng, T. P. Cotter, P. Kaghazchi, T. Jacob, B. Frank, K. Schlichte, W. Zhang, D. S. Su, F. Schüth, and R. Schlögl, Experimental and theoretical investigation of molybdenum carbide and nitride as catalysts for ammonia decomposition, *J. Am. Chem. Soc.* **135**, 3458 (2013).
- [65] E. J. McGuire, Atomic *M*-shell Coster-Kronig, Auger, and radiative rates, and fluorescence yields for Ca-Th, *Phys. Rev. A* **5**, 1043 (1972).

- [66] R. P. Gupta and S. K. Sen, Calculation of multiplet structure of core p -vacancy levels. II, *Phys. Rev. B* **12**, 15 (1975).
- [67] P. Zimmermann, S. Peredkov, P. M. Abdala, S. DeBeer, M. Tromp, C. Müller, and J. A. Van Bokhoven, Modern x-ray spectroscopy: XAS and XES in the laboratory, *Coord. Chem. Rev.* **423**, 213466 (2020).
- [68] G. Greczynski, D. Primetzhofer, J. Lu, and L. Hultman, Core-level spectra and binding energies of transition metal nitrides by non-destructive x-ray photoelectron spectroscopy through capping layers, *Appl. Surf. Sci.* **396**, 347 (2017).
- [69] A. Jana, R. J. Choudhary, and D. M. Phase, Mott-Hubbard type insulating nature of epitaxial LaVO_3 thin films, *Phys. Rev. B* **98**, 075124 (2018).
- [70] B. Alling, T. Marten, and I. A. Abrikosov, Effect of magnetic disorder and strong electron correlations on the thermodynamics of CrN, *Phys. Rev. B* **82**, 184430 (2010).
- [71] P. A. Bhohe, A. Chainani, M. Taguchi, T. Takeuchi, R. Eguchi, M. Matsunami, K. Ishizaka, Y. Takata, M. Oura, Y. Senba *et al.*, Evidence for a correlated insulator to antiferromagnetic metal transition in CrN, *Phys. Rev. Lett.* **104**, 236404 (2010).
- [72] D. Gall, C. S. Shin, R. T. Haasch, I. Petrov, and J. E. Greene, Band gap in epitaxial NaCl-structure CrN(001) layers, *J. Appl. Phys.* **91**, 5882 (2002).
- [73] A. Herwadkar and W. R. L. Lambrecht, Electronic structure of CrN: A borderline Mott insulator, *Phys. Rev. B* **79**, 035125 (2009).
- [74] M. Magnuson, M. Mattesini, C. Höglund, I. A. Abrikosov, J. Birch, and L. Hultman, Electronic structure investigation of the cubic inverse perovskite Sc_3AlN , *Phys. Rev. B* **78**, 235102 (2008).
- [75] A. S. Botana, F. Tran, V. Pardo, D. Baldomir, and P. Blaha, Electronic structure of CrN: A comparison between different exchange correlation potentials, *Phys. Rev. B* **85**, 235118 (2012).
- [76] G. J. Snyder and E. S. Toberer, Complex thermoelectric materials, *Nat. Mater.* **7**, 105 (2008).
- [77] C. X. Quintela, F. Rivadulla, and J. Rivas, Thermoelectric properties of stoichiometric and hole-doped CrN, *Appl. Phys. Lett.* **94**, 152103 (2009).
- [78] S. Kerdsonpanya, N. Van Nong, N. Pryds, A. Žukauskaite, J. Jensen, J. Birch, J. Lu, L. Hultman, G. Wingqvist, and P. Eklund, Anomalously high thermoelectric power factor in epitaxial ScN thin films, *Appl. Phys. Lett.* **99**, 232113 (2011).
- [79] S. Sumithra, N. J. Takas, D. K. Misra, W. M. Nolting, P. F. P. Poudeu, and K. L. Stokes, Enhancement in thermoelectric figure of merit in nanostructured Bi_2Te_3 with semimetal nano-inclusions, *Adv. Energy Mater.* **1**, 1141 (2011).